RSC Advances

PAPER

View Article Online
View Journal | View Issue

Cite this: *RSC Adv.*, 2024, **14**, 1367

Bismuth ferrite based acetone gas sensor: evaluation of graphene oxide loading†

Pandurang Ghadage,[a] K. P. Shinde,[b] Digambar Nadargi,[*ac] Jyoti Nadargi,[d] Hamid Shaikh,[e] Mohammad Asif Alam,[f] Imtiaz Mulla,[g] Mohaseen S. Tamboli,[h] J. S. Park[*b] and Sharad Suryavanshi[*a]

Received 4th October 2023
Accepted 18th December 2023

DOI: 10.1039/d3ra06733e

rsc.li/rsc-advances

We report a $BiFeO_3$/graphene oxide (BFO/GO) perovskite, synthesized using a CTAB-functionalized glycine combustion route, as a potential material for acetone gas sensing applications. The physicochemical properties of the developed perovskite were analysed using XRD, FE-SEM, TEM, HRTEM, EDAX and XPS. The gas sensing performance was analysed for various test gases, including ethanol, acetone, propanol, ammonia, nitric acid, hydrogen sulphide and trimethylamine at a concentration of 500 ppm. Among the test gases, the developed BFO showed the best selectivity towards acetone, with a response of 61% at an operating temperature of 250 °C. All the GO-loaded BFO samples showed an improved gas sensing performance compared with pristine BFO in terms of sensitivity, the response/recovery times, the transient response curves and the stability. The 1 wt% GO-loaded $BiFeO_3$ sensor showed the highest sensitivity of 89% towards acetone (500 ppm) at an operating temperature of 250 °C. These results show that the developed perovskites have significant potential for use in acetone gas sensing applications.

1. Introduction

Industrial development has had an important role worldwide in improving our social, cultural and economic arenas. However, it has also led to a large daily requirement for energy. The release of dangerous gases and vapours into the environment has resulted in air pollution, which is a major problem in many nations.[1] Gases such as nitrous oxide (NO_x), sulphur dioxide (SO_2), carbon monoxide (CO), hydrogen sulphide (H_2S) and volatile organic compounds (VOCs) are the main causes of air pollution.[2–8] Fig. 1 illustrates the destructive effects of air pollution on the environment. There is a proven link between air pollution and an increase in cardiovascular disease death rates of up to 20%. About 92% of the world's population lives in metropolitan areas that exceed the World Health Organization's recommended levels of air pollution. This highlights the need for an increase in the monitoring and management of gaseous air pollutants.

The detection of blood-borne VOCs in exhaled breath as a consequence of metabolic alterations or pathological illnesses is important in non-invasive medical diagnostics. As indicators of conditions like diabetes and halitosis, the levels of acetone in exhaled human breath have the potential to provide useful information for the early identification of these diseases. Bismuth ferrite (BFO) perovskites have the potential to sense acetone.[9–11] Because this ternary oxide consists of two cations of different sizes, BFO perovskites exhibit more stable and reliable gas sensing characteristics than binary metal oxides such as ZnO, CuO, WO_3 and SnO_2.[12–17] The unique surface reactivity, oxygen adsorption and relatively narrow band gap (2.19 eV) of BFOs are beneficial for increasing gas selectivity, decreasing the dependence of sensor signals on humidity to negligible levels, facilitating the transport of valence electrons and speeding up recovery times.[18,19]

Significant efforts have been dedicated to the production of nanostructured $BiFeO_3$, including nanoparticles, nanofibres and thin films,[20–24] for gas sensor research. Gas sensitivity studies of $BiFeO_3$ have been expanded to include a diverse range of target gases, such as VOCs (methanol, ethanol, acetone, benzene, toluene, glycol and gasoline), sulphur dioxide, oxygen, ammonia and formaldehyde.[20–26] $BiFeO_3$ gas sensors have demonstrated a sensitivity of 8–50 ppm for ethanol and 25 ppm for acetone, as reported in ref. 20 and 21, respectively. Nevertheless, the sensitivity of $BiFeO_3$ to ammonia and sulphur

[a]School of Physical Sciences, Punyashlok Ahilyadevi Holkar Solapur University, Solapur, 413255, India. E-mail: digambar_nadargi@yahoo.co.in; sssuryavanshi@rediffmail.com

[b]Department of Materials Science and Engineering, Hanbat National University, Daejeon, 34158, South Korea. E-mail: jsphb@hanbat.ac.kr

[c]Centre for Materials for Electronics Technology, C-MET, Thrissur, 680581, India

[d]Department of Physics, Santosh Bhimrao Patil College, Mandrup, Solapur, 413221, India

[e]SABIC Polymer Research Centre, Department of Chemical Engineering, King Saud University, P.O. Box 800, Riyadh 11421, Saudi Arabia

[f]Center of Excellence for Research in Engineering Materials (CEREM), King Saud University, P.O. Box 800, Riyadh 11421, Saudi Arabia

[g]Former Emeritus Scientist (CSIR), NCL, Pune, 411008, India

[h]Korea Institute of Energy Technology (KENTECH), 21 KENTECH-gil, Naju, Jeollanam-do, 58330, Republic of Korea

† Electronic supplementary information (ESI) available. See DOI: https://doi.org/10.1039/d3ra06733e

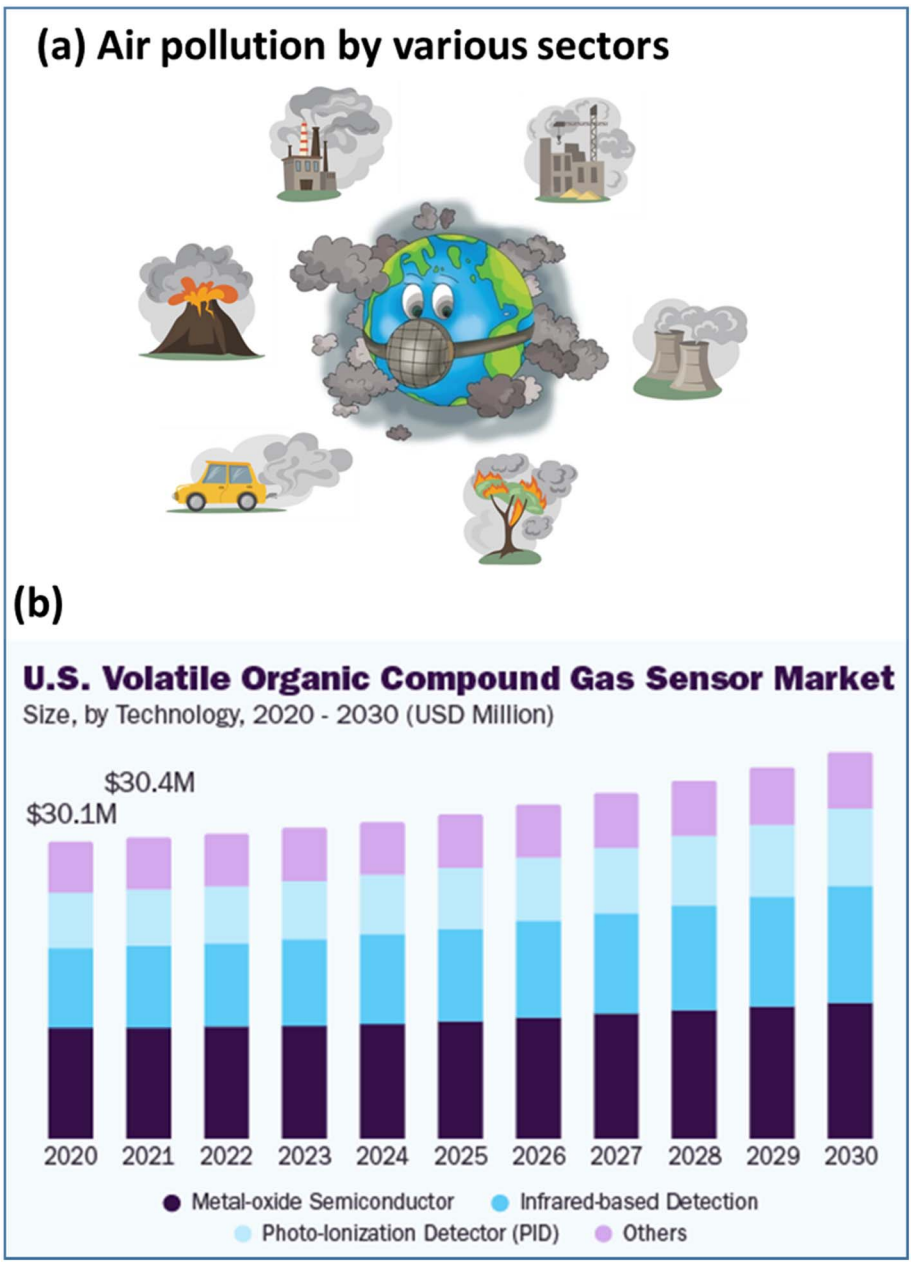

Fig. 1 (a) Schematic illustration of the destructive effects of air pollution on the environment. (b) Size of the markets for different types of gas sensor (https://www.grandviewresearch.com/).

dioxide is minimal.[22,25] Research has shown that particular surface properties significantly influence the enhancement of gas sensitivity characteristics.

Graphene oxide (GO) is a potential candidate for improving the gas sensing properties of metal oxides. The motivation for loading GO on BFO is due to its fascinating catalytic redox reactions, which cause faster adsorption and desorption of oxygen molecules over the metal oxide. If the BFO is optimised in association with GO, the gas sensing response of the parent material (*i.e.* BFO) will increase. It is expected that interactions at the interface of the BFO and GO will positively favour the effective migration of charge carriers and therefore the overall gas sensing performance will be improved.

We have elucidated a facile and flexible strategy of fabricating $BiFeO_3$ *via* a citrate sol–gel auto-combustion process. Two important aspects were considered to enhance the gas sensing properties of BFO: (1) the use of the surfactant CTAB, which facilitates a high surface area; and (2) loading with GO. We describe here the glycine sol–gel auto-combustion route, along with the physico-chemical and gas sensing properties of $BiFeO_3$ perovskites.

2. Experimental

The AR grade chemicals, such as bismuth nitrate ($Bi(NO_3)_3 \cdot 5H_2O$), ferric nitrate ($Fe(NO_3)_3 \cdot 9H_2O$), CTAB, GO and glycine,

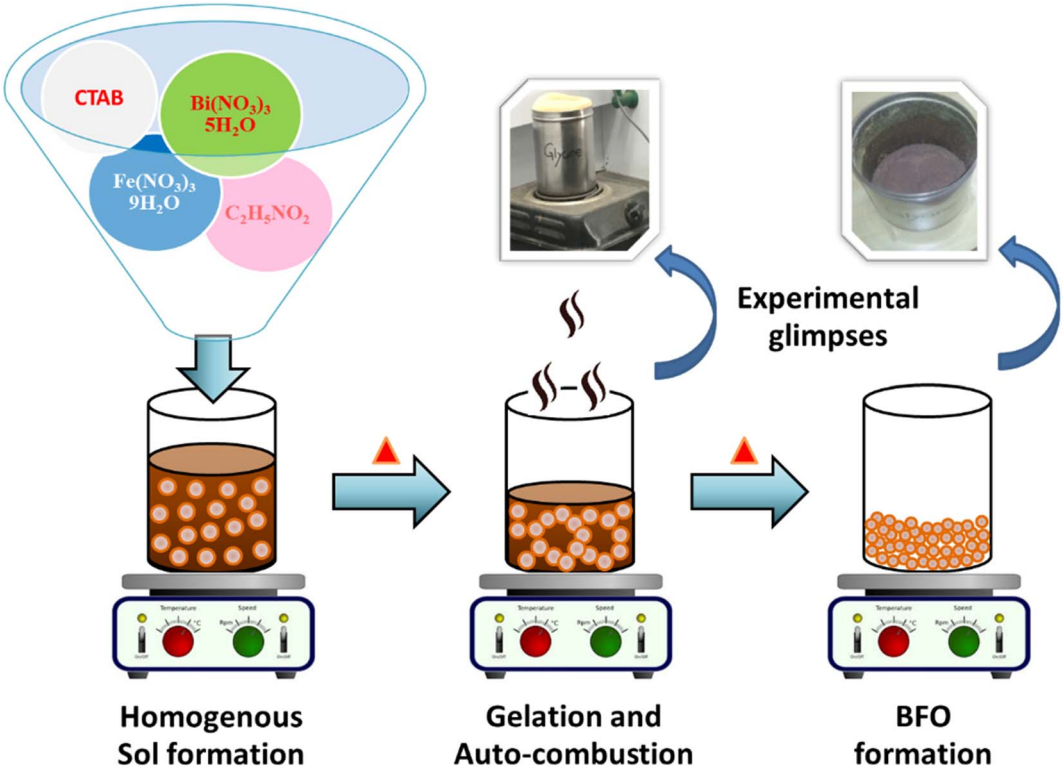

Fig. 2 Schematic diagram of the experimental protocol to develop BFO perovskite.

were used without further purification. The facile synthesis of BFO nanoparticles was achieved *via* a glycine-assisted combustion route using metal nitrates as precursors, glycine ($C_2H_5NO_2$) as a fuel and hexadecyltrimethylammonium bromide ($CH_3(CH_2)15N(Br)(CH_3)_3$) (CTAB) as a cationic surfactant. The stoichiometry of the redox mixture for combustion was calculated based on the total oxidizing and reducing valence of the oxidizer and reductant (1 : 3 mol) and was kept constant. Bismuth nitrate (24.25 g), ferric nitrate (20.2 g) and glycine (16.04 g) were well mixed in 100 mL of distilled water. The reaction mixture was stirred for 15 min until it became homogeneous. The temperature of solution was gradually increased to 100 °C. The highly viscous sol reached the percolation threshold and formed a reddish gel enriched with water. The resultant gel was then heated to >200 °C. The viscous gel began frothing and, after the evaporation of water, underwent a fast, flameless auto-combustion reaction with the evolution of large amounts of gaseous products, after which it auto-ignited to give pristine BFO as the end-product.

The CTAB-assisted BFO samples were prepared by exactly the same synthesis strategy, but with the addition of CTAB (0.12 g) to the solution at a molar ratio of surfactant/bismuth of 0.1 (Fig. 2).[27] Correspondingly, in the GO-loaded BFO synthesis process, the as-prepared BFO/CTAB powder (10 g) was dispersed in 10 mL of ethanol with rigorous stirring for 10 minutes before adding GO (0.5–1.5 wt%, steps of 0.5). This solution was ultrasonicated for 10 minutes to give a uniform dispersion of GO in BFO/CTAB. The homogeneous solution was stirred continuously at 70 °C until a dry powder was obtained. The characterization of the developed perovskite, its pellet preparation and gas sensing analysis are discussed in detail in the ESI† (I–III).

3. Results and discussion

The XRD patterns of $BiFeO_3$- and GO-loaded $BiFeO_3$ powder are shown in Fig. 3. The high-intensity peaks at $2\theta = 22.4°$, 31.7°,

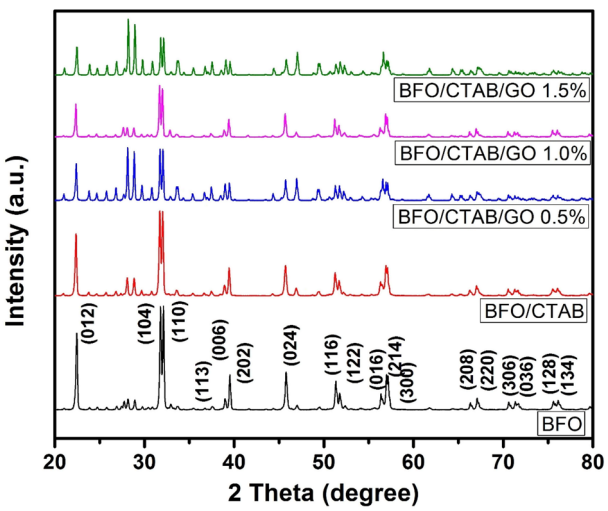

Fig. 3 XRD patterns of the developed BFO and the CTAB- and GO-modified BFOs.

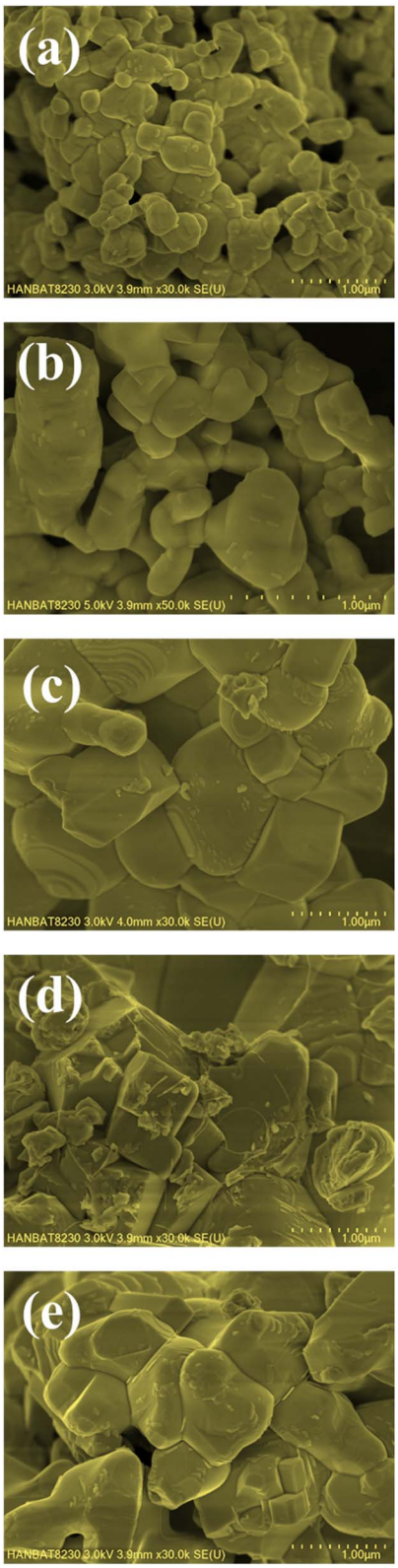

Fig. 4 FE-SEM images of (a) pristine BFO, (b) CTAB-BFO, (c–e) 0.5–1.5 wt% GO-loaded BFO.

32.0°, 39.4°, 45.7°, 51.7°, 56.3° and 56.90° are due to diffracted X-rays from the (012), (104), (110), (006), (024), (122), (018) and (214) planes, respectively. The XRD pattern of the prepared sample matched well with previously reported work and JCPDS card 86-1518, confirming the rhombohedral phase. A low-intensity peak at $2\theta = 28°$ was observed due to the formation of a secondary phase. The average crystallite size of the $BiFeO_3$ nanoparticles was 55 nm, as calculated by the Debye–Scherrer formula:[28]

$$D = \frac{k\lambda}{\beta \cos \theta} \quad (1)$$

where D = average crystallite size, $k = 0.9$, λ= wavelength of the X-rays, β = full-width half-maxima and θ = diffraction angle.

In the SEM micrographs (Fig. 4a–e), the developed nanomaterial appears as an agglomeration of semi-cuboid nanoparticles with an average grain size of 300 nm. The size of the nanoparticles increased with the incorporation of GO in BFO. Deformation in the cubic shape occurred at higher concentrations of GO (*i.e.* 1.5%).

EDAX analysis was conducted to verify the presence of the constituent elements in BFO (Fig. 5). The elemental composition of the BFO sample spectrum consists of 58.02 wt% Bi, 19.90 wt% Fe and 22.08 wt% O. The corresponding weight percent and atomic percent values of the elements in the BFO sample are tabulated in Fig. 5. The homogeneous formation of BFO was validated through elemental mapping (Fig. 5).

The colloidal backbone/networking structure of the $BiFeO_3$ is clearly visible in the TEM images (Fig. 6a and b) and the cuboid nanoparticles of GO/BFO, along with the presence of graphene sheets, was confirmed (Fig. 6d and e). This structure facilitates numerous channels for the efficient and rapid diffusion of gases and thereby improves the potential for gas sensing applications. The average particle size of ~300 nm matched well with size calculated from the SEM analysis. The HRTEM fringes (Fig. 6c and f) matched with BFO planes belonging to the rhombohedral crystal phase, thus validating the results obtained from the XRD analysis.

The elements present in the prepared sample of BFO-GO (1% GO) were determined by XPS. The XPS survey spectrum is shown in Fig. 7a. The dominant peaks present at binding energies of 160, 284, 530 and 710 eV confirm the elemental composition of Bi, C, O and Fe, respectively. The high-resolution spectra of Bi, C, O and Fe are shown separately in the Fig. 7b–e. Two separate peaks were observed for Bi $4f_{5/2}$ and Bi $4f_{7/2}$ at binding energies of 163.55 and 157.84 eV, respectively (Fig. 7b). The overlapping peaks of Fe $2P_{3/2}$ at 709.2 and 710.6 eV were resolved using convolution fitting of the graph (Fig. 7c). The Fe $2P_{1/2}$ peak was detected at 723.2 eV. The peaks at 528.7 and 529.3 eV corresponding to the O 1s group (Fig. 7d) were due to lattice oxygen and oxygen vacancies, respectively. The peaks at 284.1 and 288.2 eV in Fig. 7e correspond to C 1s, which confirms the GO loading.[29]

3.1 Gas sensing analysis

The gas sensing proficiency of the developed materials towards various reducing gases, including ethanol, acetone, propanol, ammonia, nitric acid, hydrogen sulphide and trimethylamine, was examined. In the general sensing process of metal oxide-

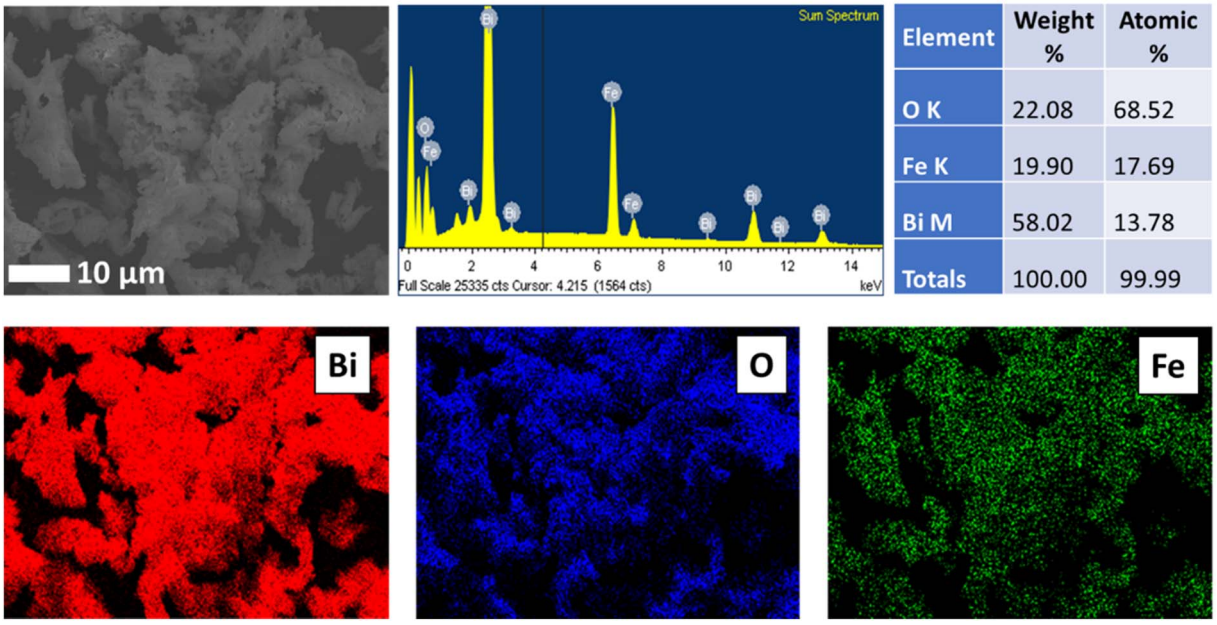

Element	Weight %	Atomic %
O K	22.08	68.52
Fe K	19.90	17.69
Bi M	58.02	13.78
Totals	100.00	99.99

Fig. 5 EDAX results and mapping of $BiFeO_3$.

based acetone gas sensors, oxygen molecules with a high electron affinity (0.43 eV) are adsorbed onto the sensor's surface and extract electrons from the detecting layer. Depending on the operating temperature, several different oxygen ion species will be present on the gas surface. The choice of gas species for testing is contingent upon the sensing material and the temperature at which sensing occurs. Typically, molecular ions are stable below 150 °C, but other species remain stable at elevated temperatures. Electron abstraction and the p-type characteristics of the gas sensor result in the formation of

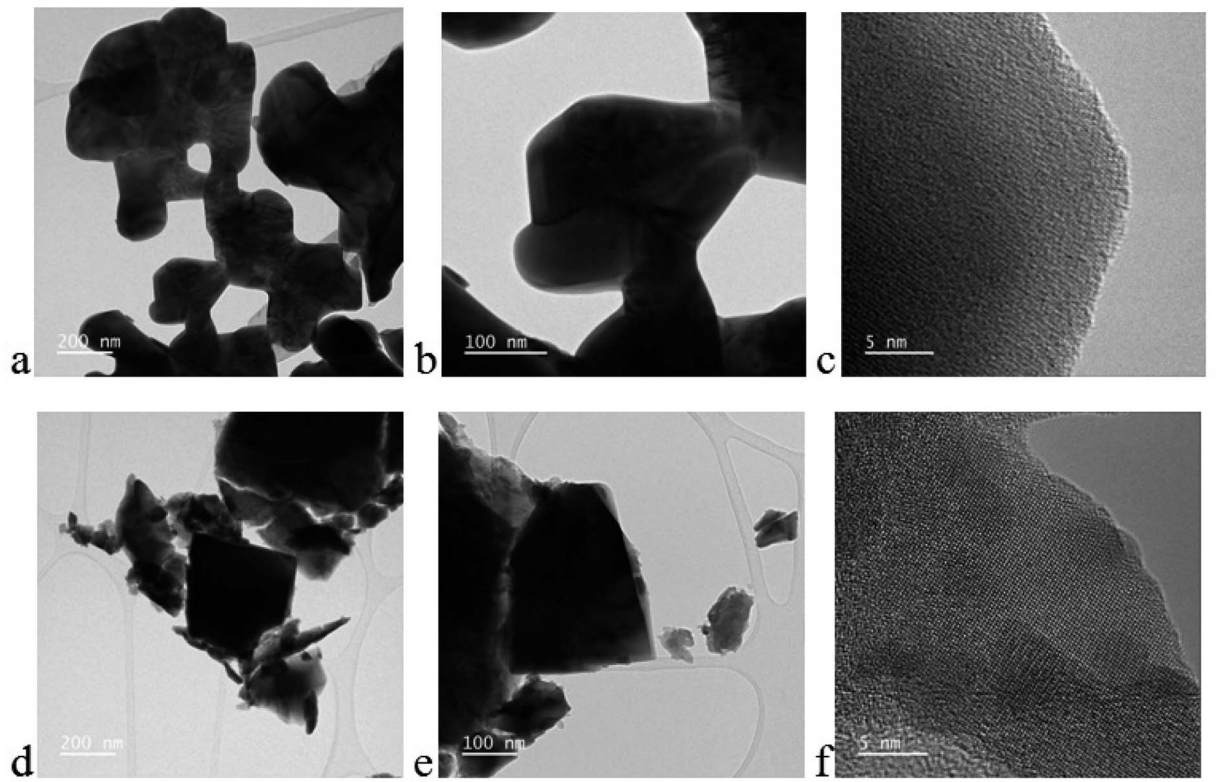

Fig. 6 TEM images of pristine (a–c) CTAB-BFO and (d–f) 0.1 wt% GO-loaded BFO.

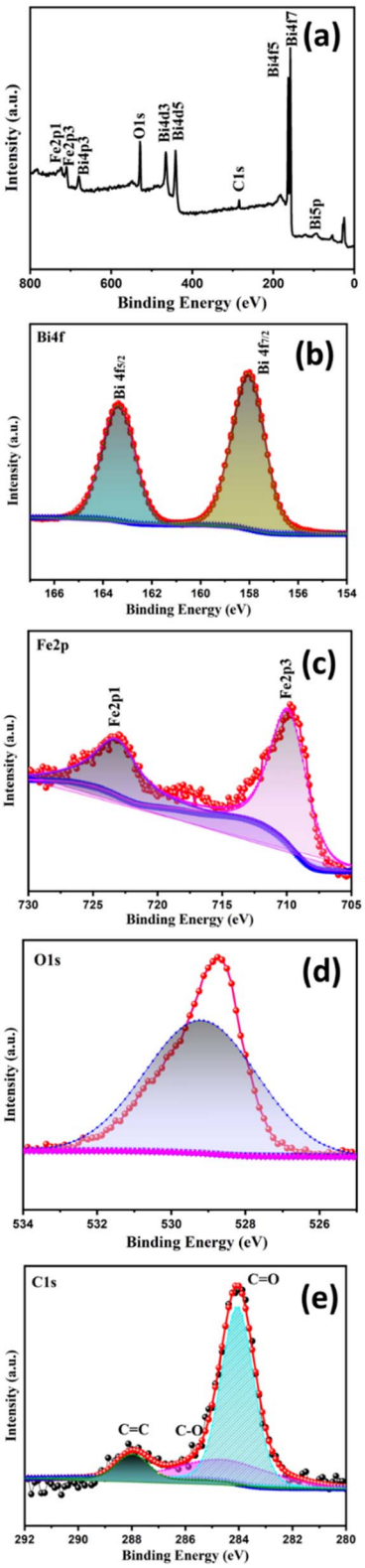

Fig. 7 XPS spectra of 1% GO-loaded BFO – (a) survey spectrum, (b–e) spectra of Bi, Fe, O and C, respectively.

a hole accumulation layer on its surface. As a result of the prevalence of holes as charge carriers in p-type gas sensors, the resistance of these sensors is lower than that of a vacuum.

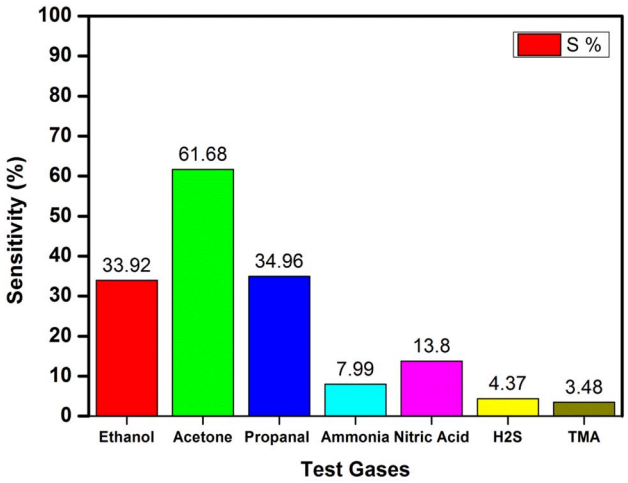

Fig. 8 Selectivity of the BFO sensor for various oxidizing and reducing gases.

Upon the injection of acetone gas into the gas test chamber, a reaction occurs with the pre-existing oxygen ions that have been adsorbed, resulting in the release of electrons (*e.g.* for acetone):

$$(CH_3COCH_3)_g \rightarrow (CH_3COCH_3)_{ads} \quad (2)$$

$$(CH_3COCH_3)_{ads} + 8O^- \rightarrow 3CO_2 + 3H_2O + 8e^- \quad (3)$$

Among the various test gases, it was observed that BFO exhibited the highest selectivity towards acetone (Fig. 8). Notably, at an operating temperature of 250 °C and a gas concentration of 500 ppm, the sensor gave a response of 61%. By contrast, none of the other test gases had a >50% response when subjected to same gas concentration and operating temperature.

Although the developed sensor had the ability to detect alcohols (propanol and ethanol), its sensitivity was low compared with acetone. Both alcohols and acetone are classified as reducing gases. Consequently, an increase in oxygen vacancies would have a positive impact on the detection of both alcohols and acetone. Despite exhibiting a favourable reaction to alcohols (ethanol, 33.92%; propanol, 34.96%), the sensitivity of the BFO nanoparticles to alcohols was significantly inferior to their sensitivity to acetone (61.68%). This selectivity towards acetone is attributed to the reactivity of the target gas with the sample or to the bond energy. The selectivity and sensitivity of the sensor can be determined by the bond energy of the gas analyte under certain conditions, whereas under other conditions the chemical reactivity of the gas analyte with the effective sample surface becomes crucial. The behaviour of the organic vapour varies depending on the operating temperature due to the preferential adsorption of oxygen towards acetone at a specific temperature. The sensor's selectivity towards acetone vapour makes it a promising candidate for many applications involving acetone sensing, especially the non-invasive monitoring of diabetes through exhaled breath. The following

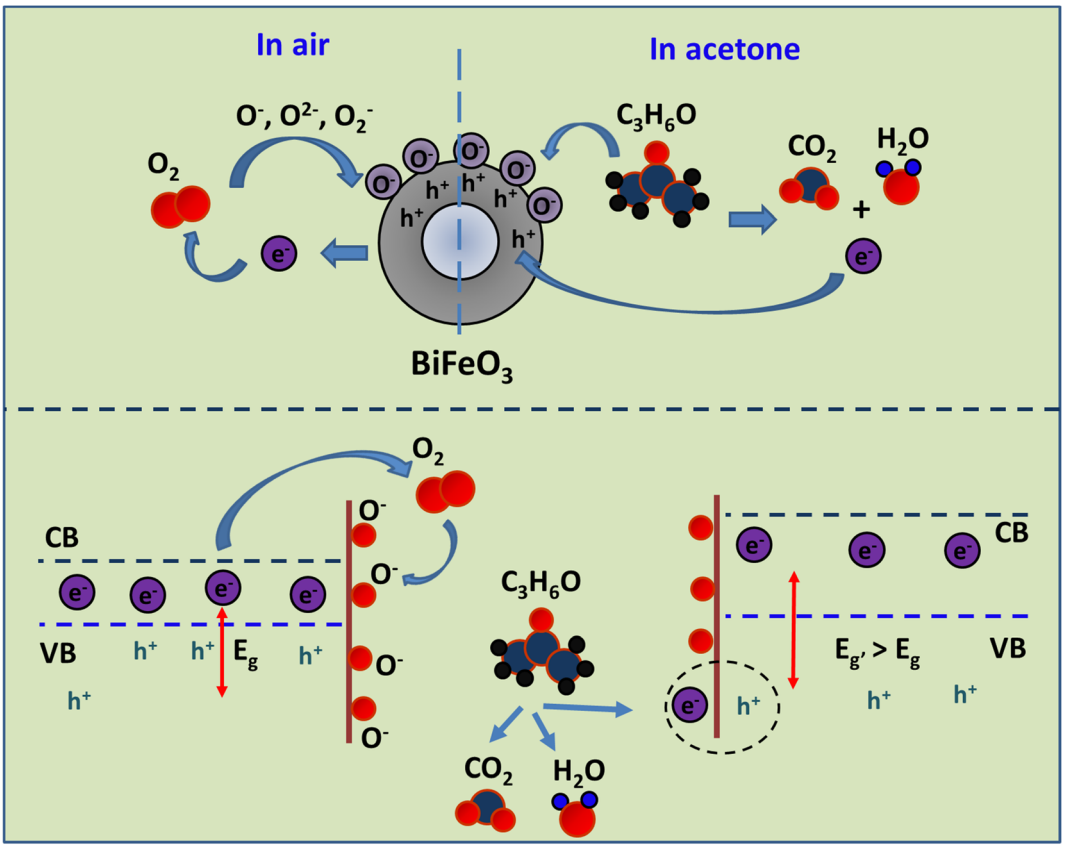

Fig. 9 Schematic illustration of the response mechanism of $BiFeO_3$ towards acetone gas.

section discusses the gas sensing mechanism of bismuth ferrite nanoparticles towards acetone (Fig. 9).

Fig. 10 is a graphical representation of the gas response in relation to the operating temperature for pristine BFO, BFO/CTAB and BFO/CTAB/GO (0.5–1.5 wt%) specifically targeting 500 ppm acetone. The analysis demonstrates that all the samples exhibit a sharp sensitivity with increasing temperature. However, the sensitivity of the samples decreases above a certain threshold temperature.[30] The sample of 1 wt% GO-loaded BFO/CTAB exhibited a greater sensitivity of 89.44% at an operating temperature of 250 °C than the other samples.

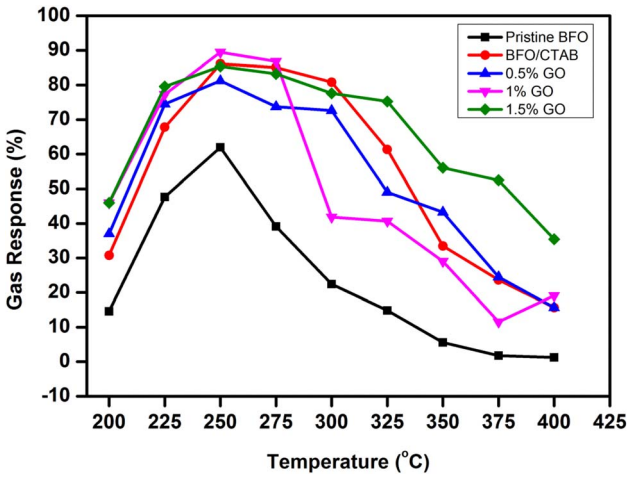

Fig. 10 Response to acetone as a function of operating temperature.

When the sensors are exposed to air, oxygen molecules are adsorbed onto the surface of sensor to form chemisorbed oxygen species (O_2^-, O^- or O^{2-}). These species are formed by capturing the electrons present on the adsorption sites of the oxide surface:

$$O_{2(gas)} \leftrightarrow O_{2(ads)} \quad (4)$$

$$O_{2(ads)} + e^- \leftrightarrow O_{(ads)}{}^{2-} \quad (5)$$

$$O_{(ads)}{}^{2-} + e^- \leftrightarrow 2O_{(ads)}{}^- \quad (6)$$

$$O_{(ads)}{}^- + e^- \leftrightarrow O_{(ads)}{}^{2-} \quad (7)$$

The oxygen ions mainly exist in the form of O^- in the temperature range 100–300 °C, which is the general operating temperature. Above this, O^{2-} ions are directly incorporated into the lattice. A sufficient number of oxygen molecules form an electron-depleted space-charge layer on the surface of the nanoplates. This steady concentration of oxygen donates a basic electrical resistance in air. When the sensor is exposed to an oxidizing gas (*e.g.* NO_x), the molecules of NO_X capture electrons from the conduction band and react with the adsorbed oxygen ion, leading to the formation of adsorbed NO^{2-} ions.

The reactions can be written as follows:

$$NO_{2(gas)} + e^- \leftrightarrow NO_{2(ads)}^- \quad (8)$$

$$NO_{2(gas)} + O_{2(ads)}^- + 2e^- \leftrightarrow NO_{2(ads)}^- + 2O^- \quad (9)$$

The decrease in the electron concentration on the surface of the material, followed by an increase in the width of the depletion layer results in an increase in the resistance of the sensor. When exposure to NO_X stops, the NO_2^- ions are desorbed and recovery occurs. This cycle continues and NO_X detection takes place.

$$NO_{2(ads)}^- + 2O^- + e^- \leftrightarrow NO_{2(gas)} + 2O_{(ads)}^{2-} \quad (10)$$

If the sensor is exposed to a reducing gas (*e.g.* ammonia), the gas interacts with the pre-adsorbed oxygen species, which results in a decrease in the concentration of surface oxygen species, leading to a decrease in the resistance of the sensor:

$$CO_{(gas)} \leftrightarrow CO_{(ads)} \quad (11)$$

$$CO_{(ads)} + O^- \leftrightarrow CO_{2(gas)} + e_{(ads)}^- \quad (12)$$

The sensors exhibited a pronounced increase their response during the early phase (1–200 ppm) as a result of varying concentrations of the target gas (acetone). Gradual saturation occurred when the concentration was increased further (Fig. 11). This may be attributed to the decreasing availability of active surfaces, which hinders the potential interaction between the gas and the sensing material.

The transient response (response/recovery behaviour) is a crucial parameter of sensors for practical applications. Fig. 12 shows the transient response curve for the 1 wt% GO-loaded BFO/CTAB sensor. The measurements were carried out at an operating temperature of 250 °C and 500 ppm acetone. The 1 wt% GO-loaded BFO/CTAB sensor sample showed a rapid response time of 38 s and a recovery time of 1 min. The other sensors also responded in a decent manner. Table 1 gives the response/recovery times for all the developed sensors.

In terms of stability, the optimised sensor (1 wt% GO-loaded BFO/CTAB) demonstrated a stability of about 98% of its original performance over a span of 60 days when exposed to 500 ppm acetone (Fig. S2†). This is strong evidence for the durability and repeatability of the sensor in the context of commercial applications.

We used the present perovskite ($BiFeO_3$) as an example to compare chemiresistive perovskites with metal–organic frameworks (MOFs) and covalent organic frameworks (COFs) (Tables 2 and 3). MOFs and COFs are novel and developing categories of materials characterized by self-assembled porous network structures. These structures consist of organic linkers connecting metal nodes. These materials have the potential to be used as electrochemical sensors for the detection of diverse target gases, including biomolecules. This is because they have

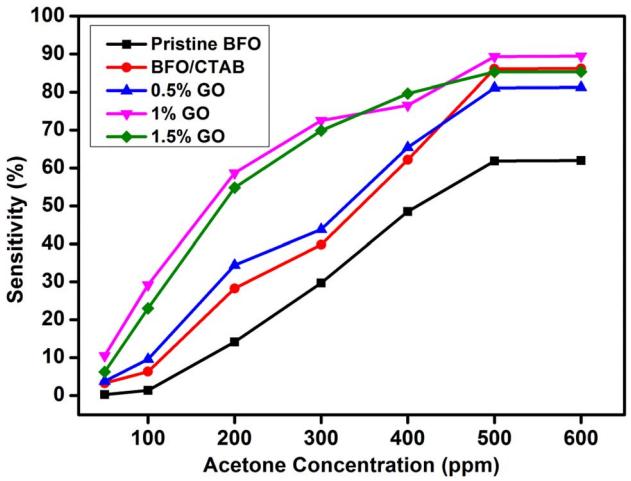

Fig. 11 Response of the sensor towards different concentrations of acetone at 250 °C.

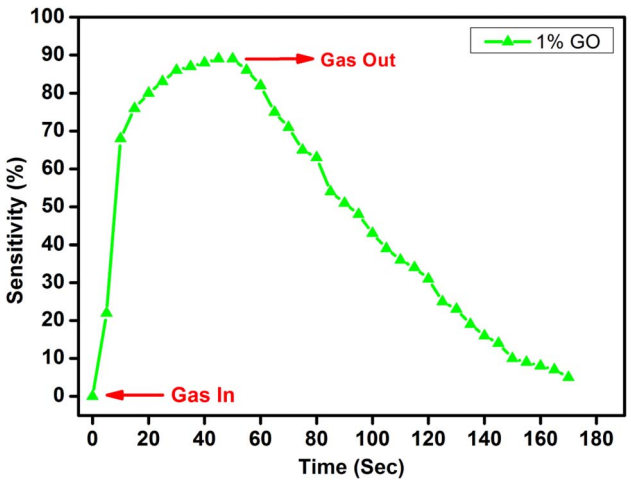

Fig. 12 Transient response characteristics of the 1 wt% GO-loaded BFO/CTAB sensor at 250 °C.

Table 1 Transient response (response/recovery behaviour) of the developed sensors

Sample ID	Response (sensitivity%)	Response time	Recovery time
BFO	61.98	1′ 58″	2′ 22″
CTAB/BFO	86.12	38″	1′ 2″
0.5 wt% GO	81.22	55″	1′ 18″
1.0 wt% GO	89.44	48″	1′ 35″
1.5 wt% GO	85.00	45″	1′ 52″

Table 2 Chemiresistive MOFs/COFs for the detection of inorganic and organic molecules

MOF/COF	Target gas	Detection limit (ppm)	Ref.
$Cu_3(HITP)_2$	NH_3	0.5	31
$Ni_3(HHTP)$	NO	0.1	32
	H_2S	1	
ZIF-67	CH_2O	5	33
$Co(Im)_2$	Me_3N	2	34

Table 3 Comparative chart of sensor parameters of developed $BiFeO_3$ with state of art publications

Sensing material	Operating temperature (°C)	Concentration	Selectivity	Sensitivity	Response and recovery times (s)	Reference
$BiFeO_3$ NPs	340	0.1 vol%	Acetone	$R_g/R_a = 10$	40–80	35
$BiFeO_3$ NPs	350	10 ppm	Acetone	$R_g/R_a = 12$	—	36
1 wt% Pd/$BiFeO_3$ NPs	300	500 ppm	Acetone	$(R_g - R_a)/R_a = 83.4$	75–104	37
GO/$BiFeO_3$ NPs	250	500 ppm	Acetone	$(R_g - R_a)/R_a = 89.4$	48–95	Present work

a wide surface area, a diverse pore structure that can be regulated, increased functionality and unique catalytic activities.

4. Conclusions

We developed BFO/GO perovskites *via* a CTAB-functionalized glycine combustion route. The developed perovskite was tested for its gas sensing performance towards various oxidizing and reducing gases. Crystallographic identification of the perovskites confirmed a rhombohedral phase with an average nanoparticle crystallite size of 55 nm. The microstructural and morphological characterizations established that the incorporation of CTAB and GO in the BFO synthesis influenced the surface morphology and particle size of BFO, dramatically changing the gas sensing performance of the sensors. The sensor with 1 wt% GO-loaded CTAB/BFO showed a higher selective sensitivity of 89% towards acetone (500 ppm at 250 °C) than pristine BFO. The response and recovery times were 48 s and 1 min, which is quite fast compared with other GO-loaded BFO samples. These results show that the 1 wt% GO-loaded CTAB/BFO material can be used to fabricate an effective acetone sensor.

Conflicts of interest

There are no conflicts to declare.

Acknowledgements

The authors extend their appreciation to the Deputyship for Research and Innovation, "Ministry of Education" in Saudi Arabia for funding this research (IFKSUOR3-108-2).

References

1 I. Manisalidis, E. Stavropoulou, A. Stavropoulos and E. Bezirtzoglou, *Front. Public Health*, 2020, **8**, 14, DOI: 10.3389/fpubh.2020.00014.
2 J. Qiu, X. Hu, X. Min, W. Quan, R. Tian, P. Ji, H. Zheng, W. Qin, H. Wang, T. Pan, S. Cheng, X. Chen, W. Zhang and X. Wang, *ACS Appl. Mater. Interfaces*, 2020, **12**(17), 19755–19767.
3 D. Y. Nadargi, R. B Dateer, M. S. Tamboli, I. S. Mulla and S. S. Suryavanshi, *RSC Adv.*, 2019, **9**, 33602–33606.
4 H. Xu, J. Li, P. Li, J. Shi, X. Gao and W. Luo, *ACS Appl. Mater. Interfaces*, 2021, **13**(41), 49194–49205.
5 G. Jung, S. Hong, Y. Jeong, W. Shin, J. Park, D. Kim and J.-H. Lee, *ACS Appl. Mater. Interfaces*, 2022, **14**(15), 17950–17958.
6 S. S. Mehta, D. Y. Nadargi, M. S. Tamboli, L. S. Chaudhary, P. S. Patil, I. S. Mullad and S. S. Suryavanshi, *Dalton Trans.*, 2018, **47**, 16840–16845.
7 D. Y. Nadargi, M. S. Tamboli, S. S. Patil, R. B. Dateer, I. S. Mulla, H. Choi and S. S. Suryavanshi, *ACS Omega*, 2020, **5**(15), 8587–8595.
8 K. Phasuksom, W. Prissanaroon-Ouajai and A. Sirivat, *RSC Adv.*, 2020, **10**, 15206–15220.
9 X. Yang, H. Li, L. Tai, Z. Li, W. Wu, C. Zhou, P. Sun, F. Liu, Y. Xu, Y. Gao, X. Liang and G. Lu, *Sens. Actuators, B*, 2018, **282**, 339.
10 H. Xu, J. Xu, H. Li, W. Zhang, Y. Zhang and Z. Zhai, *J. Mater. Res. Technol.*, 2022, **17**, 1955–1963.
11 Q. Li, W. Zhang, C. Wang, J. Ma, L. Ning and H. Fan, *RSC Adv.*, 2018, **8**, 33156–33163.
12 Y. Xue-Lian, Y. Wang, Y.-M. Hu, C.-B. Cao and H. L.-W. Chan, *J. Am. Ceram. Soc.*, 2009, **92**, 3105.
13 H. Obayashi, Y. Sakurai and T. Gejo, *J. Solid State Chem.*, 1976, **17**, 299–303.
14 G. Dong, H. Tian and J. Fang, *RSC Adv.*, 2015, **5**, 29618–29623.
15 D. Y. Nadargi, M. S. Tamboli, S. S. Patil, *et al.*,, *SN Appl. Sci.*, 2019, **1**, 1564.
16 S. Steinhauer, Gas Sensors Based on Copper Oxide Nanomaterials: A Review, *Chemosensors*, 2021, **9**, 51.
17 C. Dong, R. Zhao, L. Yao, R. Yan, X. Zhang and Y. Wang, *J. Alloys Compd.*, 2020, **820**, 153194.
18 B. Li, Q. Zhou, S. Peng and Y. Liao, *Front. Chem.*, 2020, **8**, 321.
19 H. Kim and J. Lee, *Sens. Actuators, B*, 2014, **192**, 607–627.
20 X.-L. Yu, Y. Wang, Y.-M. Hu, C.-B. Cao and H. L.-W. Chan, *J. Am. Ceram. Soc.*, 2009, **92**, 3105.
21 G. Dong, H. Fan, H. Tian, J. Fang and Q. Li, *RSC Adv.*, 2015, **5**, 29618.
22 S. Das, S. Rana, S. M. Mursalin, P. Rana and A. Sen, *Sens. Actuators, B*, 2015, **218**, 122.
23 M. Sobhan, Q. Xu, A. Katoch, F. Anariba, S. S. Kim and P. Wu, *Nanotechnology*, 2015, **26**, 175501.
24 M. Norayr, *Sensor Test Conferences*, vol. 749, 2011.
25 M. Dziubaniuk, R. Bujakiewicz-Korońska, J. Suchanicz, J. Wyrwa and M. Rękas, *Sens. Actuators, B*, 2013, **188**, 957.
26 T. Tong, J. Chen, D. Jin and J. Cheng, *Mater. Lett.*, 2017, **197**, 160–162.
27 X. Deng, C. Song, Y. Tong, G. Yuan, F. Gao, D. Liu and S. Zhang, *Phys. Chem. Chem. Phys.*, 2018, **20**, 3648–3657.

28 P. A. Ghadage, L. K. Bagal, D. Y. Nadargi, R. C. Kambale and S. S. Suryavanshi, *Mater. Today: Proc.*, 2021, **43**(4), 2725–2729.
29 P. Scherrer, *Nachr. Ges. Wiss. Göttingen*, 1918, **26**, 98–100.
30 E. Massera, V. L. Ferrara, M. Miglietta, T. Polichetti, I. Nasti and G. Francia, Gas sensors based on graphene, *Chem. Today*, 2011, **29**, 39–41.
31 M. G. Campbell, D. Sheberla, S. F. Liu, T. M. Swager and M. Dincă, *Angew. Chem., Int. Ed.*, 2015, **54**, 4349.
32 M. K. Smith and K. A. Mirica, *J. Am. Chem. Soc.*, 2017, **139**, 16759.
33 E.-X. Chen, H. Yang and J. Zhang, *Inorg. Chem.*, 2014, **53**, 5411.
34 E.-X. Chen, H.-R. Fu, R. Lin, Y.-X. Tan and J. Zhang, *ACS Appl. Mater. Interfaces*, 2014, **6**, 22871.
35 A. S. Poghossian, H. V. Abovian, P. B. Avakian, V. Mkrtchian and M. Haroutunian, *Sens. Actuators, B*, 1991, **9**, 545–549.
36 S. Chakraborty and M. Pal, *J. Alloys Compd.*, 2019, **787**, 1204–1211.
37 P. Ghadage, K. Pavan, D. Nadargi, S. Patil, M. Tamboli, N. Bhandari, I. Mulla, C. Park and S. Suryavanshi, *Ceram. Int.*, 2023, **49**(4), 5738–5747.